# Nanobubbles at GPa pressure under graphene

| | |
|---|---|
| Journal: | *Nano Letters* |
| Manuscript ID: | nl-2015-024756.R1 |
| Manuscript Type: | Communication |
| Date Submitted by the Author: | n/a |
| Complete List of Authors: | Zamborlini, Giovanni; Università degli Studi di Trieste, Department of Physics<br>Imam, Mighfar; ICTP, Applied Physics<br>Patera, Laerte; Università degli Studi di Trieste, Department of Physics<br>Menteş, Tevfik; Elettra - Sincrotrone Trieste S.C.p.A,<br>Stojić, Nataša; Abdus Salam International Centre of Theoretical Physics,<br>Africh, Cristina; IOM-CNR, Laboratorio TASC<br>Sala, Alessandro; Elettra - Sincrotrone Trieste S.C.p.A,<br>Binggeli, Nadia; Abdus Salam International Centre for Theoretical Physics,<br>Comelli, Giovanni; University of Trieste, Physics<br>Locatelli, Andrea; Elettra - Sincrotrone Trieste S.C.p.A., |
| | |

# Nanobubbles at GPa pressure under graphene

Giovanni Zamborlini,[†,‡] Mighfar Imam,[¶] Laerte Luigi Patera,[†,§]
Tevfik Onur Menteş,[‖] Nataša Stojić,[*,¶,⊥] Cristina Africh,[§] Alessandro Sala,[‖]
Nadia Binggeli,[¶,⊥] Giovanni Comelli,[†,§] and Andrea Locatelli[*,‖]

*Department of Physics, University of Trieste, Via Valerio 2, I-34127 Trieste, Italy, Peter Grünberg Institute (PGI-6) and JARA-FIT, Research Centre Jülich, 52425 Jülich, Germany, Abdus Salam International Centre for Theoretical Physics, Strada Costiera 11, Trieste I-34151, Italy, IOM-CNR Laboratorio TASC, S.S. 14 km 163.5 in AREA Science Park, Basovizza, I-34149 Trieste, Italy, Elettra - Sincrotrone Trieste, S.S. 14 km 163.5 in AREA Science Park, Basovizza, I-34149 Trieste, Italy, and IOM-CNR Democritos, Trieste I-34151, Italy*

E-mail: nstojic@ictp.it; andrea.locatelli@elettra.eu

## Abstract

We provide direct evidence that irradiation of a graphene membrane on Ir with low-energy Ar ions induces formation of solid noble-gas nanobubbles. Their size can be controlled by thermal treatment, reaching tens of nm laterally and height of 1.5 nm upon annealing at 1080 °C. Ab-initio calculations show that Ar nanobubbles are subject to pressures reaching tens of GPa, their formation being driven by minimization of the energy cost of film distortion and loss of adhesion.

---

[*] To whom correspondence should be addressed

[†] Department of Physics, University of Trieste, Via Valerio 2, I-34127 Trieste, Italy

[‡] Peter Grünberg Institute (PGI-6) and JARA-FIT, Research Centre Jülich, 52425 Jülich, Germany

[¶] Abdus Salam International Centre for Theoretical Physics, Strada Costiera 11, Trieste I-34151, Italy

[§] IOM-CNR Laboratorio TASC, S.S. 14 km 163.5 in AREA Science Park, Basovizza, I-34149 Trieste, Italy

[‖] Elettra - Sincrotrone Trieste, S.S. 14 km 163.5 in AREA Science Park, Basovizza, I-34149 Trieste, Italy

[⊥] IOM-CNR Democritos, Trieste I-34151, Italy

**Keywords:** graphene, nanobubbles, argon, ion-irradiation, implantation, ripening.

With both Young's modulus and third-order elastic stiffness reaching the terapascal range, graphene has emerged as the strongest material ever measured.[1] Together with the high flexibility provided by the nature of $sp^2$ carbon bond, these outstanding properties make graphene the ideal candidate for ultra-thin impermeable membranes separating different environments. For instance, graphene-based windows have been successfully employed in environmental cells for electron microscopy, paving the way to the spectroscopic investigation of liquids.[2–4] Remarkably, graphene membranes are able to trap mesoscopic volumes of gas in nanobubbles (NB), demonstrating suitability for gas-storage applications and extreme robustness, even at single layer thickness.[5] NB have recently sparked intense research interest due to their intriguing properties and have been observed in various systems, ranging from epitaxial graphene grown on 4H-SiC[6] to graphene on $SiO_2$.[7] Formation of NB under graphene has also been reported upon high temperature heating of the graphene-diamond interface,[8] with application as anvil cells for high-pressure reactions inaccessible under ambient conditions, *e.g.* the polymerization of buckminster-fullerene.[9] Importantly, the large lattice deformation occurring in NB permits to strain-engineer the local electronic and magnetic properties of the film.[10] It has been shown that strain generated by NB under graphene can induce Landau levels arising from pseudo-fields of 300 tesla.[11,12] The peculiar film morphology induced by NB is also known to induce optical bistability in graphene, which may find application in nano-devices enabling giant optical nonlinearity[13]

To date, only few pioneering studies have addressed the basic structural properties of NB under graphene using surface science methods. A systematic picture on the subject is still missing, aggravated by the lack of model systems targeting NB formation and growth. Indeed, the characterization of such an entangled system poses extraordinary experimental challenges owing to limited access to buried species. Recently, graphene and hexagonal boron-nitride (h-BN) on transition metals came in the spotlight, providing the initial ground for studying film deformations resulting from irradiation with low energy noble gas ions. On Rh(111), both graphene and h-BN have been shown capable of trapping individual Ar atoms under the distorted lattice-mesh.[14] Intercalated atoms form characteristic dome-like protrusions, opening the door to a strain-mediated functionalization of the film.[15,16] A recent STM study demonstrated that the intercalation of oxygen under graphene/Ru causes moiré blisters to transform in NB, their size, shape and density being controlled by the extent of the oxidation treatment.[12] Further, a recent work on graphene on Ir(111) reports nucleation and growth of flat nanoplatelets following $Ar^+$ irradiation and subsequent annealing, which have been attributed to intercalated C.[17]

By adopting advanced electron and scanning probe microscopy methods, we have investigated the morphology and spatial distribution of Ar intercalated under graphene on Ir(100), specifically addressing the formation of NB and their thermal stability. Ar was chosen because, being inert, it does not either chemisorb to Ir or react off graphene. We intercalated it using low energy ion irradiation, causing minimal damage to the graphene lattice while ensuring an initially uniform lateral distribution. Our substrate, Ir(100) offers the advantage of tunable film-substrate interaction, favouring diffusion of intercalated atoms at temperatures higher than 500 °C, when the film completely decouples from the substrate;[18,19] similar to Ru(0001) and Ir(111),[20,21] it also warrants that the intercalated atoms are sealed under graphene, due to substrate chemisorption of the graphene's island edges. Combined use of low energy electron microscopy (LEEM)[22] and synchrotron-based photoemission electron microscopy (XPEEM)[23] gave us access to the interface structure and composition. Thanks to high sensitivity to near-surface species, XPEEM allowed mapping the lateral distribution of intercalated Ar and its evolution upon annealing. The corrugations induced in the film were quantitatively characterized using scanning tunneling microscopy (STM). The experiments were corroborated by ab-initio simulations, which clarify the physical mechanisms governing ripening of intercalated species.

We grew graphene on the (100) face of Ir by chemical vapor deposition of ethylene at sample temperature nearing 850 °C,[19] interrupting deposition after micron-size islands had developed. The specimen was then irradiated at room temperature with low energy Ar ions, as detailed in the Methods Section. Sputtering energies in the range $0.1 - 0.5$ kV were used to maximize cross section for intercalation, while minimizing damage and implantation into Ir bulk.[24] The LEEM and LEED images in Figure 1(a) illustrate the state of the graphene/Ir interface before and after irradiation. As can be seen, unirradiated graphene exhibits the characteristic stripes resulting from alternating domains of physisorbed-flat (FG) and buckled graphene (BG) phases.[18] In the latter phase $\sim 10\%$ of the carbon atoms is chemisorbed to the substrate, originating large one-dimensional nanoripples exhibiting periodicity of 2.1 nm.[18,25] After irradiation, the electron reflectivity diminishes notably at the island, which appears darker than its surroundings. Note also the dramatic change in the LEED pattern, where the graphene spots are not discernible and the diffuse background is very high. STM measurements reveal that this is due to a remarkably rough surface morphology, see Figure 1(b). Nevertheless, the film appears to be continuous, even if point defects show up at atomic resolution. Interestingly, XPEEM spectra of Ar *2p* core level emission shown in Figure 1(c) demonstrate that the Ar signal comes exclusively from the graphene islands. This, together with the relatively small effective attenuation length of Ar *2p* electrons at the kinetic energy used in the experiments (178 eV), suggests that Ar emitters are likely trapped at the graphene/Ir interface and not below, in agreement with recent literature on ion-irradiated graphene.[24,26,27] Under the typical irradiation fluences used in this work, we estimate that about 0.1 $\mathrm{eML_{Ir}}$ (equivalent monolayer of the unreconstructed Ir(100) surface, see Methods) of Ar is implanted at the graphene/Ir interface, see supplementary information (SI).

The evolution of the surface morphology upon consecutive temperature treatments is illustrated in Figure 2. Each treatment consisted of a ramp to a set temperature, subsequently kept for 5 minutes, followed by cooling down to room temperature. In the final treatment, temperatures close to 1080 °C were reached. Figure 2(a) shows an STM image of graphene

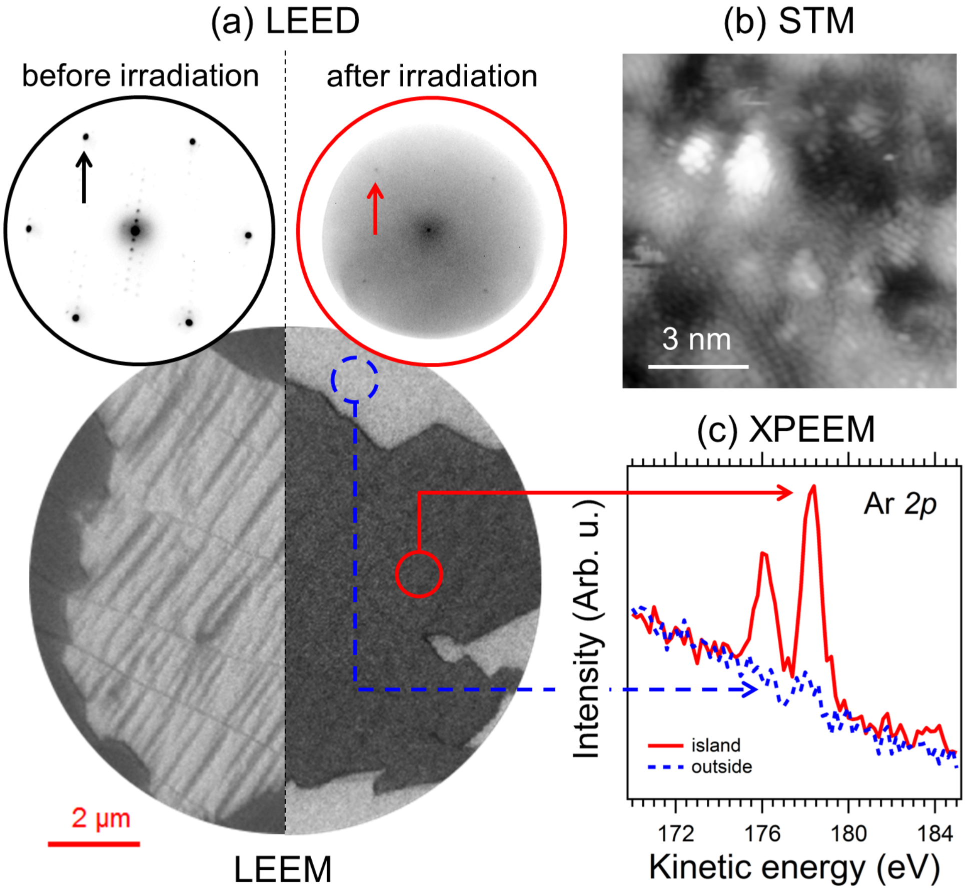

Figure 1: (a, top) room temperature LEED patterns at $V_{start} = 38$ V of graphene on Ir(100) before and after Ar$^+$ irradiation (0.5 kV at $1.5 \cdot 10^{-5}$ mbar for 7 s; $F = 1.6 \cdot 10^{14}$ atoms/cm$^2$); the pattern on the left exhibits strong graphene first order spots (one is marked by a black arrow); After irradiation they disappear, the Ir first order spot becoming barely visible (red arrow); (a,bottom) Room temperature LEEM images at $V_{start} = 12$ V of the same surface. The bright (dark) stripes on the left correspond to the FG (BG) phase on Ir(100).[18] After irradiation, the graphene island appears darker then the surrounding Ir, due to a dramatic decrease of the electron reflectivity. (b): room temperature STM image of the graphene surface after a similar treatment; image size $10 \times 10$ nm$^2$ ($V_b = 0.1$ V; $I_t = 5$ nA); (c) XPEEM Ar *2p* spectra acquired from distinct regions inside and outside the graphene island shown in (a). Photon energy: 420 eV.

right after irradiation at 80 °C. The bright dots are protrusions with median height of about 0.10 nm. Figure 2(b-e) shows the variations occurring in film morphology upon annealing. As can be seen, the bright spots become larger and decrease in number, manifesting the occurrence of a ripening process observed in STM and LEEM (see movies in SI). Often, the NB are trapped at step edges (see Figure 2e), consistent with previous STM work reporting NB nucleation and growth at defect sites.[12] After the final treatment, the lateral size of the observed structures is typically few nm, often surpassing 10 nm. Quantitative analysis of the STM data shows that the protrusions' median height increases from 0.10 up to 1.5 nm upon annealing to 1080 °C (see SI). The decrease in spot density is accompanied by the development of large areas of FG. Upon cooling, BG is found to preferentially nucleate close to the protrusions. It is plausible that the formation of BG provides an energetically-favorable configuration to accommodate the strain around the protrusions.[18] Yet, we note that the BG phase has no role in the ripening process occurring upon annealing.[28]

To further characterize the state of the interface, we microscopically probed the Ar *2p* and C *1s* core level emission within micrometer-sized graphene islands. We note that, above 600 °C, the C *1s* emission recovers a narrow line-shape (not shown), suggesting that defects heal close to graphene growth temperatures. The Ar *2p* emission shows instead two spin-split doublet components, see Figure 2(f). We assign the low and high binding energy (BE) components to dispersed intercalated Ar, in the form of isolated atoms / two-dimensional aggregates (labeled 2D in the figure), and three-dimensional (3D) clusters, respectively. Such interpretation is consistent with a previous photoemission study on Ar NB embedded in Si and $\alpha$-$Al_2O_3$.[29] The inspection of the spectra in Figure 2(f) reveals a clear transition from 2D to 3D character upon annealing. As shown in Figure 2(g), the sum of the 2D and 3D components is almost constant up to 700 °C. The subsequent decrease in intensity is compatible with self-screening effects, following the significant increase of the protrusion height evidenced by our STM data. As quantitatively determined in a fit, both components shift to higher BEs upon annealing, with a particularly large shift for the 3D component.

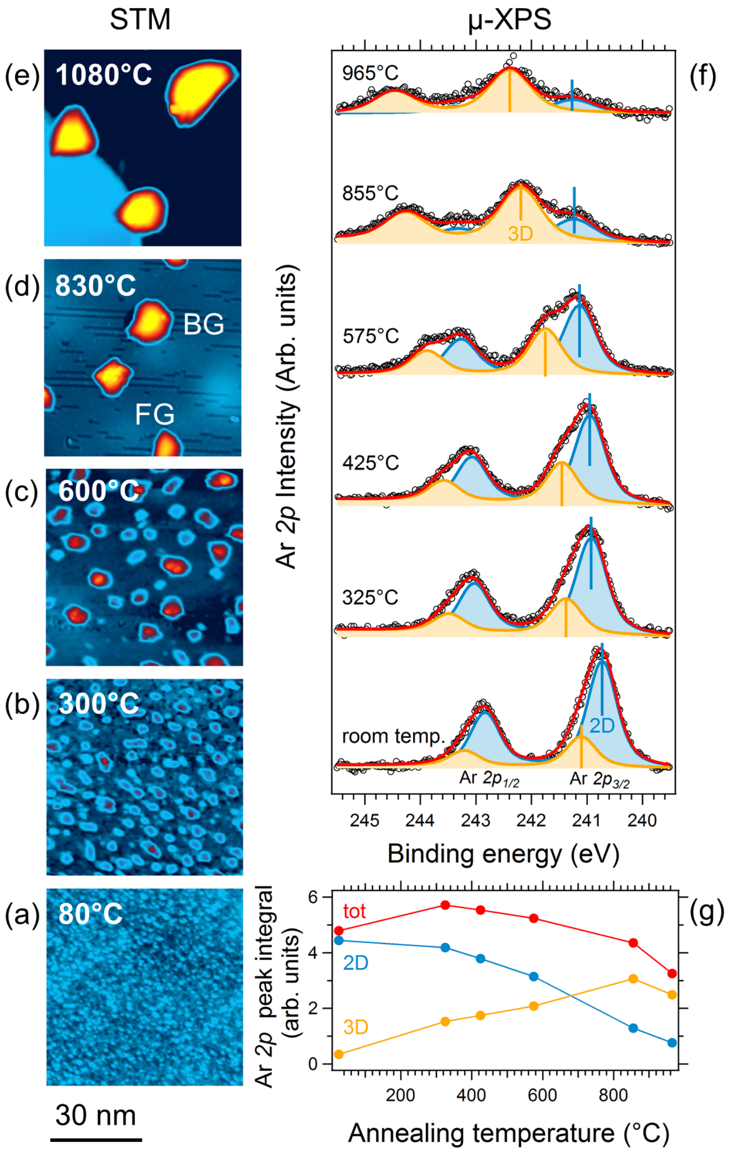

Figure 2: (left) The STM topographs illustrate the evolution of the film morphology upon annealing (temperatures are indicated by the labels). All images, measured at room temperature, have size of 65 × 65 nm$^2$; (a) after 15 s Ar$^+$ irradiation at 0.15 kV, $V_b = -0.2$ V; $I_t = 0.7$ nA (b) $V_b = -0.9$ V; $I_t = 0.5$ nA (c) $V_b = -0.2$ V; $I_t = 1$ nA (d) $V_b = -0.2$ V; $I_t = 1$ nA; the stripes close to the protrusions identify the BG phase. (e) $V_b = -0.2$ V; $I_t = 1$ nA (f) room temperature $\mu$-XPS Ar $2p$ spectra from a single, well-defined graphene island after Ar$^+$ irradiation (0.1 kV, 420 s at $2 \cdot 10^{-5}$ mbar Ar; $F = 1.4 \cdot 10^{15}$ atoms/cm$^2$) and subsequent annealing (temperatures are indicated by labels); Voigt lineshape best fits (red curves) are superimposed to the experimental data (empty circles). The low and high binding energy doublets correspond to 2D (blue) and 3D (orange) interfacial Ar respectively. The vertical bars provide a guideline highlighting the shift in binding energy. The peak integrals are shown in (g). The red dots correspond to the total Ar signal. Photon energy: 400 eV.

Similar effects have already been observed for noble-gas NB in Al.[29,30] They are interpreted as due to variations in the electron screening of the metal in response to the core-hole in the photoemission final state. Importantly, such variations are dependent on the NB radius, suggesting a relationship between BE variation and bubble size.[31]

Figure 3(a,b) shows room temperature LEEM and PEEM images of a graphene island after thermal treatment to 1050 °C. In (a), the bright and neutral grey regions correspond to the FG and BG phases, respectively. We interpret the small dots, highlighted by red circles, as due to regions where the film is not parallel to the surface plane. Since these features grow in size upon annealing, we identify them with the protrusions seen in STM. A few isolated wrinkles interconnecting particles are also visible, disclosing a strain relief mechanism already observed in other graphene systems.[32] In order to confirm the assignment of the particles as Ar clusters, we performed x-ray absorption spectromicroscopy (XAS-PEEM) probing the L absorption edge of Ar by measuring the secondary electron yield as a function of the photon energy. In the XAS-PEEM image in (b) the intensity is proportional to the local Ar concentration. There is a one-to-one matching between the bright features in XAS-PEEM and the spots in LEEM. Some clusters can be seen at the extreme border of the flake, which was also confirmed by STM and suggests that intercalated species cannot escape from the island even after annealing to 1080 °C. Spectra obtained from inside and outside the spots in graphene are shown in Figure 3(c). As can be seen, only the protrusions' spectra display resonances at about 245, 248 and 250 eV, in perfect accord with XAS data for gas phase Ar clusters.[33] Figure 3(d) and 3(e) allow us comparing Ar $L_3$ XAS-PEEM and Ir $4f_{7/2}$ XPEEM images. At the electron kinetic energy used for the Ir image (96 eV), the effective attenuation length is close to a minimum for most materials.[34] The remarkable inversion of contrast with Ar $L_3$ image points to the substrate emission being screened, revealing that the clusters sit above Ir. The featureless C *1s* image in (f) demonstrates instead that the protrusions are not due to multi-layer graphene, in contrast with literature data for Ir(111).[17] Combining the above, we conclude that the protrusions are Ar NB, located at the graphene/Ir interface

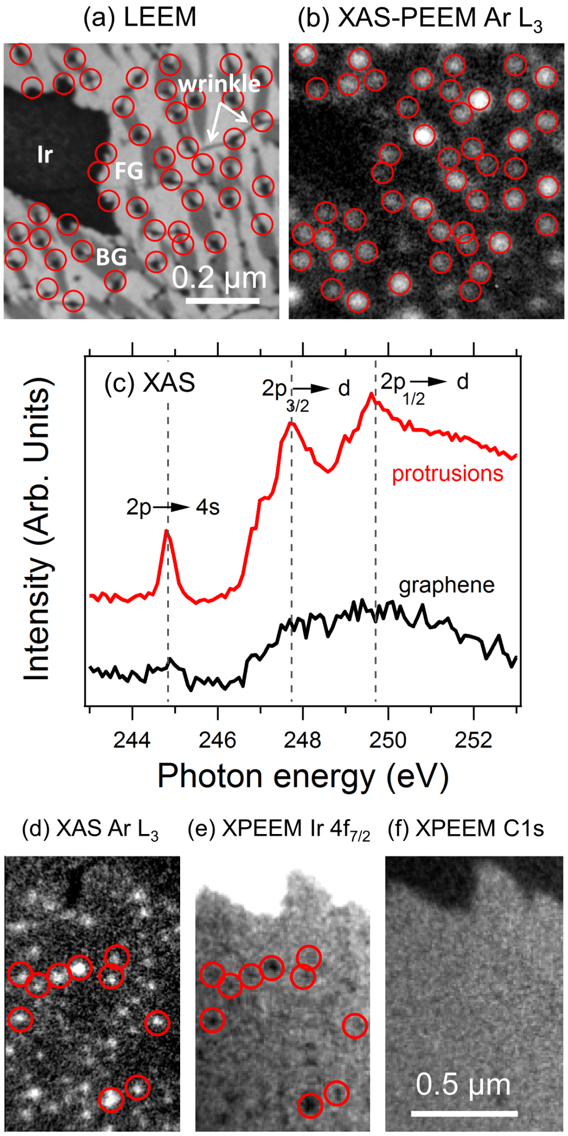

Figure 3: (a) room temperature LEEM image ($V_{start}$ = 12 V) of a graphene flake after $Ar^+$ irradiation (0.1 kV, 150 s at $1.5 \cdot 10^{-5}$ mbar Ar, $F = 7.5 \cdot 10^{14}$ atoms/cm$^2$) and subsequent annealing to 1050 °C; the black dots correspond to protrusions in the film (b) Ar $L_3$ PEEM of the same region, obtained after subtracting PEEM images acquired at 243 eV (baseline intensity) from images acquired at 247.7 eV (Ar $L_3$ edge). The intensity of the resulting image is proportional to the Ar concentration, with the bright regions corresponding to Ar clusters. Red circles have been added to facilitate comparison with (a); (c) average XAS-PEEM spectra from regions of interest inside the red circles and from FG+BG. (d) Ar $L_3$ XAS-PEEM image of another flake along with (e) Ir $4f_{7/2}$ and (f) C *1s* XPEEM images; the Ar clusters show up as bright spots in (d); the inversion of contrast in (e) is due to screening of the substrate emission by the clusters.

and not below, as may occur on softer materials.[31]

In order to unravel the physics governing the ripening of Ar, we carried out ab-initio calculations for the graphene/Ar/Ir(100) system. In the calculations, Ar single atom and mini-clusters (dimer, trimer, tetramer) were placed in a cell containing 110 iridium surface atoms and 320 carbon atoms (details are given in the Methods Section). The unit cell is shown in Figure 4(a), along with the resulting relaxed atomic configurations obtained for the intercalated Ar monomer (b), dimer (d), trimer (f) and tetramer (g). The optimized geometry used to study an Ar dimer oriented perpendicular to the surface is also shown in Figure 4(c). Structural parameters of the relaxed configurations are indicated by labels (see also SI). Note that the heights of the protrusions for the horizontal clusters are in excellent agreement with our STM data for the 2D Ar at 80 °C. Such tall protrusions are made possible by a relatively strong physisorption on Ir in the surroundings of the cluster.[25]

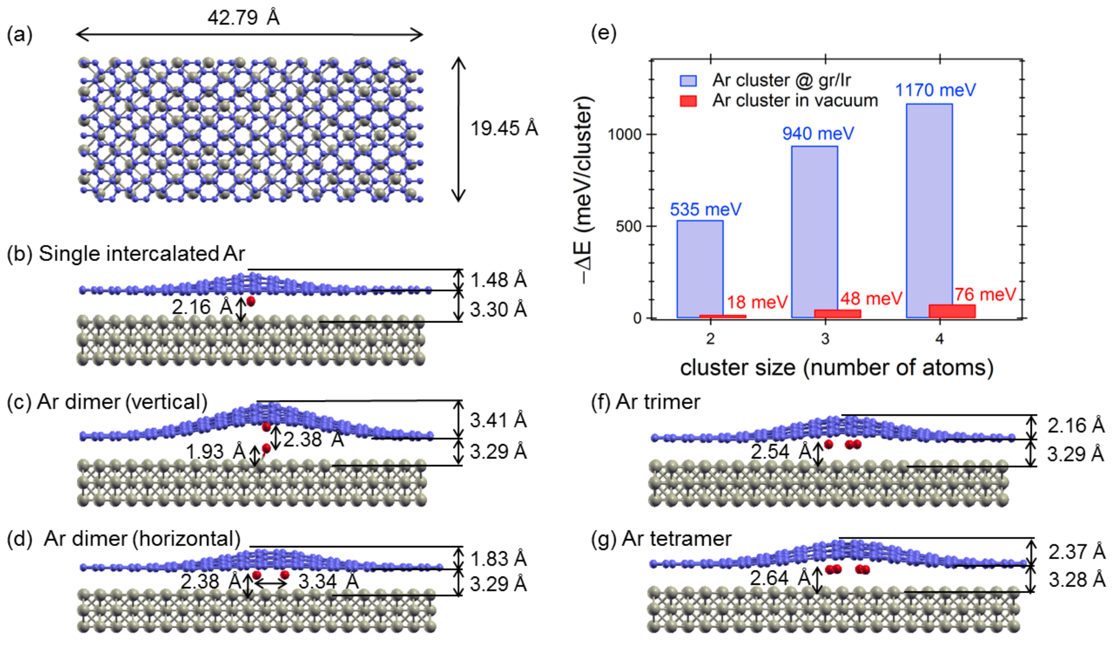

Figure 4: (a) top view of the unit cell used in our ab-initio calculations showing graphene (blue spheres) and the upper Ir layer (grey spheres). Side view of the optimized atomic geometries for (b) a single intercalated Ar (red spheres); (c) vertical and (d) horizontal Ar dimers; (f) horizontal trimer and (g) tetramer. Comparison between the energy gain when forming Ar clusters from single Ar atoms at the graphene/Ir interface ($-\Delta E^{NAr}_{gr/Ir}$, see text) and in vacuum is shown in (e).

To elucidate the origin of ripening, we calculated the formation energy of the small Ar clusters at the graphene/Ir interface, obtained as: $\Delta E^{NAr}_{gr/Ir} = E^{NAr}_{gr/Ir} - N \cdot E^{1Ar}_{gr/Ir}$, with $N = 2$ to 4 where $E^{NAr}_{gr/Ir}$ stands for the total energy of the system with an intercalated $N$-atom Ar cluster and $E^{1Ar}_{gr/Ir}$ denotes the total energy with only a single intercalated Ar atom. The associated energy gain to form a dimer, trimer, and tetramer at the graphene/Ir interface, $-\Delta E^{NAr}_{gr/Ir}$, is 535, 940 and 1170 meV, respectively (see plot in Figure 4e). The energy gain to form the corresponding free-standing relaxed Ar mini-clusters in vacuum amounts to 18, 48 and 76 meV. It is thus clear that there is a drastic increase in the energy gain at the graphene/Ir interface (factor $> 30$ for a dimer), which is related to the distortion of the physisorbed graphene.[35] In other words, there is a considerable net energy gain when two or more protrusions merge into a single, larger one. Of course, such energy gain alone is not sufficient to induce ripening. The other necessary condition is the mobility of intercalated atoms. Thus, we estimated the energy barriers for Ar diffusion between graphene and Ir by mapping the energies of a single Ar atom placed along different diffusion paths within the unit cell. Overall, the resulting energy barriers for diffusion under graphene on Ir are in the range $40 - 120$ meV (see SI). These values permit Ar aggregation already near room temperature. Indeed, this is confirmed by STM observations at 80 °C. Figure 5(a) presents an STM image of the smallest protrusion observed in experiments at very low irradiation. This shows a striking agreement in both shape (b) and intensity modulation (c) with the simulated image of an Ar tetramer below graphene (other structures are discussed in the SI). This remarkable matching confirms that Ar is trapped at the graphene/Ir interface already in the initial stages of the ripening process. Indeed, if Ar was implanted below the Ir surface, one would observe a less localized pattern, manifested by a smoother curvature of the graphene, as reported for various clean and adsorbate-covered metal surfaces.[36]

We note that the horizontal (2D) structures are the lowest-energy configurations obtained in our calculations for Ar clusters containing up to 4 atoms. As an example, we find that the Ar 3D tetramer (tetrahedron-type structure) is unstable and relaxes to the 2D arrangement, in excellent agreement with the experimental STM data in Figure 5. On the other hand, STM (Figure 2) also shows that clusters undergo a 2D to 3D transition upon ripening, suggesting that the 3D configuration is preferred for large $N$. This can be understood from the scaling behavior with $N$ of the change in strain and adhesion energy of the film: the 2D clusters induce a severe adhesion energy reduction, characterized by an unfavorable linear scaling with $N$. This makes the 2D protrusions energetically uncompetitive at large $N$ with respect to the 3D ones, which display sublinear strain and adhesion energy scaling with $N$ (see[37]).

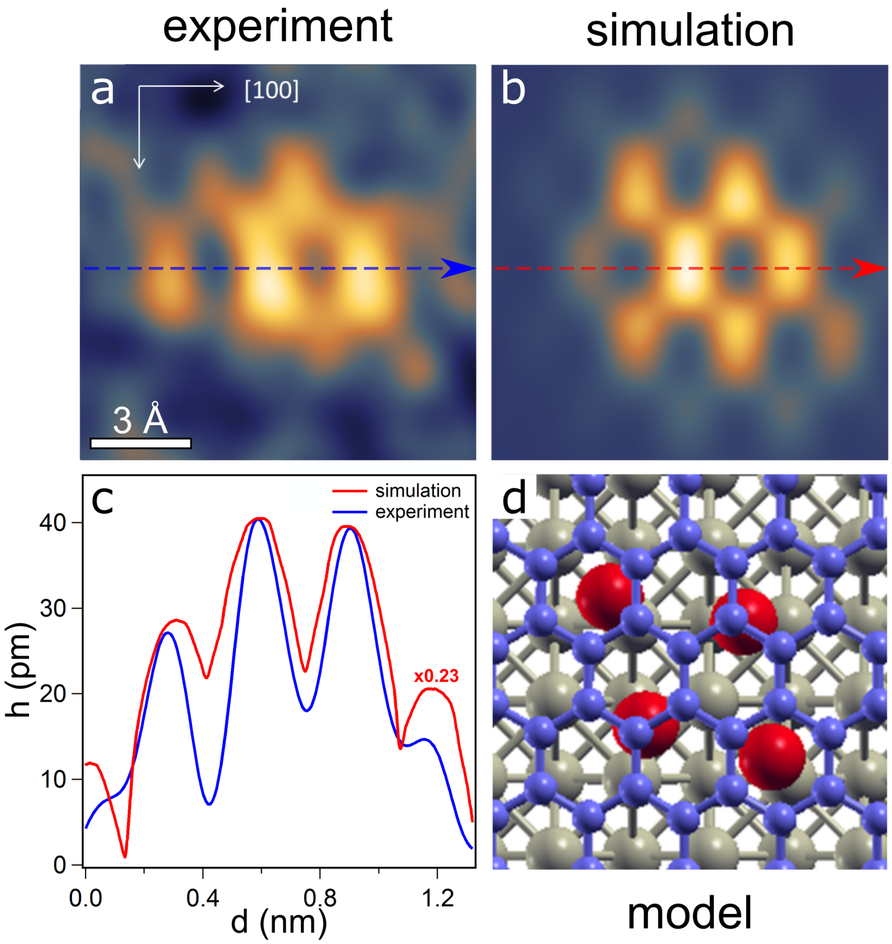

Figure 5: (a) experimental STM image of one of the smallest protrusions observed in our experiments; the surface was prepared with 5 s Ar$^+$ irradiation at 0.15 kV at sample temperature of 80 °C (1.3×1.5 nm$^2$; $V_b = 0.1$ V; $I_t = 4$ nA); (b) simulated STM image corresponding to an Ar tetramer; (c) cross sectional cuts through the experimental and simulated images along the dashed lines; the theoretical curve has been rescaled to the experimental data to facilitate comparison; (d) top view of the Ar tetramer model.

As final point, we estimate the pressure experienced by small intercalated Ar clusters at the graphene/Ir interface, based on the calculations for the Ar dimer. To this purpose, we placed the dimer at the graphene/Ir interface in two configurations, with axis perpendicular and parallel to the surface plane, see Figure 4(c,d), evaluating in both cases the bond contraction with respect to a dimer in vacuum. For the latter, the calculated equilibrium distance is 3.74 Å. For our system, the bond length contracts to 2.38 Å (3.34 Å) for the orientation perpendicular (parallel) to the surface. Already from the bond contractions, it is obvious that the forces due to the physisorbed graphene membrane are very large and anisotropic. Based on the bond contractions, the stress experienced by the Ar was estimated in two different ways. In one, we calculated the stress tensor of the strained bulk face-centred tetragonal (*fct*) Ar, imposing relative lateral and vertical bond length contractions equal to those found at the graphene/Ir interface for the horizontal and vertical dimer, respectively.[38] In the other, we directly calculated the force (in vacuum) acting on the Ar atoms when the dimer is contracted to the values found when intercalated under graphene, dividing it by the corresponding contracted *fct* surface area per Ar atom. The resulting stress components from the forces in the lateral and perpendicular directions are 3 and 70 GPa, respectively. The corresponding components calculated from the bulk Ar-*fct* stress tensor are 8 GPa and 75 GPa.[39] The estimated effective[40] pressures obtained from the two approaches (25 GPa, 30 GPa) are a factor of 3 to 30 higher than those reported for Ar NB in amorphous carbon[41] and for NB at the graphene-diamond interface.[8,9]

Considering now the large clusters observed after thermal treatment, the question arises whether they also experience high pressure conditions. A careful observation of the images in Figure 2(d,e), as well as the STM data at 400 °C (see Figure SI. 1 from SI), reveals that the observed NBs always display a polygonal shape. Owing to the high flexibility of graphene, such configuration must reflect the actual shape of underlying clusters, suggesting that Ar atoms do not form droplets but rather solid aggregates. Based on the phase-diagram data,[42] we deduce that large clusters must experience pressures well above 5 GPa, as also obtained from our *ab initio* calculations for mini-clusters. Accordingly, assuming that Ar is condensed in close-packed (fcc-like) structures, we estimate the number of Ar atoms in the NB obtaining values of the order of $10^3$ for lateral size of few tens of nm.

In conclusion, we followed the evolution of sub-ML amounts of argon implanted at the graphene/Ir(100) interface and provided direct evidence of cluster formation at and above room temperature. The larger aggregates display a lateral size up to tens of nanometers and height up to several atomic layers, producing NB in graphene containing up to few thousand Ar atoms. Intercalated Ar undergoes extreme pressure, reaching values well into tens GPa range. As discussed, the ripening process is driven by the minimization of the energy cost due to film distortion and loss of adhesion. For this reason, we expect that ripening of intercalated noble gases can also occur in other graphene/metal systems showing comparable adhesion strength, where it might be fruitfully exploited to strain-engineer the local chemical properties of graphene. We obtained similar findings in preliminary experiments on $Ne^+$-irradiated graphene on Ir(100) and $Ar^+$-irradiated graphene on Ni(111), the latter observation having been recently confirmed by Späth *et al.*.[43] Finally, we note that our study fosters the investigation of Van der Waals solids under extreme pressure and high temperatures. Indeed, rather than using molecular beams to obtain condensation, our method exploits ripening of Ar implanted under graphene, the cluster size being controlled by a simple annealing process. Thanks to the high transparency of single-layer graphene, the clusters can be investigated by means of synchrotron-based methods, similar to high-pressure environmental cells for in vivo studies using photoelectron spectroscopy.[2]

**Note added:** after submission, a related paper investigating the control of phonon excitation at graphene/Pt(111) by intercalated Ar clusters has been published.[44]

# Methods

**Sample preparation**: Ion irradiation was carried out in normal incidence using commercial sputter guns (Eurovac 981-2043 for SPELEEM experiments and SPECS IQE-11/35 for STM experiments). We carried out irradiations with 0.5 kV and 0.1 kV Ar ions at $1.5 \cdot 10^{-5}$ mbar, corresponding to an ion current $i_{Ar^+}$ of 4 and 0.6 $\mu$A, respectively. Lower sputtering energies were found to produce less damage in the film. Correspondingly, the treatment time $t$ increased from few seconds at 0.5 kV to 500 s at 0.1 kV. Under such conditions, typical fluences $F$ of $1.5 \cdot 10^{15}$ atoms/cm$^2$ were obtained (calculated as $i_{Ar^+} \cdot t/A_{beam}$, where $A_{beam}$ is the ion beam area on the sample). The Ar coverage is expressed in equivalent monolayers of the unreconstructed Ir(100) surface, eML$_{\mathrm{Ir}}$, corresponding to $\sim 1.357 \cdot 10^{15}$ atoms/cm$^2$.

**Spectroscopic photoemission and low energy electron microscopy (SPELEEM)**: The spectro-microscopic characterization was carried out using the SPELEEM microscope at the Nanospectroscopy beamline of the Elettra storage ring. This instrument combines low energy electron microscopy (LEEM) and microprobe-diffraction ($\mu$-LEED) with energy filtered x-ray photoemission electron microscopy (XPEEM).[45] Using the photon beam as probe, the microscope enables implementing laterally resolved versions of the two principal synchrotron-based spectroscopies, x-ray absorption spectroscopy (XAS) and x-ray photoemission spectroscopy (XPS). While in the former secondary electrons are used for image formation, in the latter photoelectrons emitted from core levels or the valence band are detected. The lateral resolution of the SPELEEM is about 10 nm in LEEM operation mode and below 30 nm in XAS-PEEM/XPEEM.[46,47] Along with imaging, the SPELEEM enables $\mu$-XPS and APRES to be carried out. These measurements are restricted to an area of about 2 microns in diameter, selected by means of a field-limiting aperture. In both LEEM and PEEM operation modes, the kinetic energy of electrons $E_{kin}$ is regulated by applying a voltage bias, $V_{start}$, to the sample stage, referred to as start voltage. $E_{kin} = eV_{start} - eV_{tr}$, where $V_{tr}$ indicates the voltage bias corresponding to the transition from total reflection to the backscattering regime, also known as MEM-LEEM transition. In PEEM measurements, whenever possible, the spectra were referenced to the Fermi level. Otherwise, the Ir $4f_{7/2}$ core level, bulk component was used.

**Scanning Tunneling Microscopy**: the experiments were performed at IOM-CNR TASC laboratory (Trieste) with a modified Omicron variable-temperature STM (VT-STM) in a UHV system with standard sample preparation facilities and base pressure $1 \cdot 10^{10}$ mbar. Imaging was performed in constant-current mode with tunneling current ($I_t$) ranging from 1 to 5 nA and bias voltage ($V_b$) ranging from 0.1 to 1 V for both empty ($V_b > 0$) and filled ($V_b < 0$) states. Specific $I_t$, and $V_b$ values are reported for each presented image

**Ab-initio calculations**: We have performed DFT calculations in a plane-wave basis using the PWSCF code.[48] The generalized gradient approximation (GGA) in the Perdew-Burke-Ernzerhof parametrization[49] was adopted for the exchange and correlation functional. The effects of long-range van der Waals interactions were taken into account via the semiempirical DFT-D method.[50,51] To describe the surfaces, we used supercell slab geometry. Our slab, consisting of 3 Ir monolayers (total of 330 Ir atoms), is terminated at one side with a graphene layer (320 C atoms) and 1-4 Ar intercalated atoms. Periodic Ir-slab replicas are separated by a vacuum of 14 Å. The atomic positions of the bottom two Ir layers were fixed, while the graphene, the Ar atoms and the upper Ir layer were allowed to fully relax. For the vertical Ar dimer, the lateral coordinates of two Ar atoms were constrained to be equal. Similarly, for the energy-barrier calculations, we fixed only the lateral position of the Ar atom and that of one (distant) C atom, and the bottom two Ir layers, while graphene and the rest of Ir were relaxed. The ultrasoft Vanderbilt pseudopotentials have been used.[52] We applied a kinetic-energy cutoff of 28 Ry for the plane-wave expansion of the electronic wavefunctions and of 320 Ry for the electronic charge density. The Brillouin-zone sampling was performed using the Γ k-point. We employed a Gaussian-level smearing of 0.02 Ry to determine the Fermi energy. The tunneling current in the STM simulations is evaluated within the Tersoff-Hamann approximation.[53] The STM images are generated using the constant-current condition and using an applied bias of 0.1 V.

## Acknowledgement

The authors thank C. Dri for useful discussion on STM data interpretation. GZ thanks Elettra - Sincrotrone Trieste for financial support. L.L.P. acknowledges funding from MIUR through Progetto Strategico NFFA. C.A. acknowledges support from MIUR through the program PRIN 2010-2011 - Project n° 2010N3T9M4 and the program "Progetto Premiale 2012" - Project ABNANOTECH. The calculations were performed on the FERMI (Blue gene/Q) supercomputer, thanks to the CINECA ISCRA grant IscrC_Giri.

## References

(1) Lee, C.; Wei, X.; Kysar, J. W.; Hone, J. *Science* **2008**, *321*, 385–388.

(2) Kolmakov, A.; Dikin, D.; Cote, L.; Huang, J.; Abyaneh, M.; Amati, M.; Gregoratti, L.; Günther, S.; Kiskinova, M. *Nature Nanotechnology* **2010**, *6*, 651–657.

(3) Krueger, M.; Berg, S.; Stone, D.; Strelcov, E.; Dikin, D. A.; Kim, J.; Cote, L. J.; Huang, J.; Kolmakov, A. *ACS Nano* **2011**, *5*, 10047–10054.

(4) Kraus, J.; Reichelt, R.; Gunther, S.; Gregoratti, L.; Amati, M.; Kiskinova, M.; Yulaev, A.; Vlassiouk, I.; Kolmakov, A. *Nanoscale* **2014**, *6*, 14394–14403.

(5) Stolyarova, E. et al. *Nano Letters* **2009**, *9*, 332–337.

(6) Trabelsi, A. B. G.; Kusmartsev, F. V.; Robinson, B. J.; Ouerghi, A.; Kusmartseva, O. E.; Kolosov, O. V.; Mazzocco, R.; Gaifullin, M. B.; Oueslati, M. *Nanotechnology* **2014**, *25*, 165704.

(7) Zabel, J.; Nair, R. R.; Ott, A.; Georgiou, T.; Geim, A. K.; Novoselov, K. S.; Casiraghi, C. *Nano Letters* **2012**, *12*, 617–621.

(8) Xuan Lim, C.; Sorkin, A.; Bao, Q.; Li, A.; Zhang, K.; Nesladek, M.; Loh, K. *Nature Communications* **2013**, *4*, 1556.

(9) Lim, C. H. Y. X.; Nesladek, M.; Loh, K. P. *Angewandte Chemie* **2014**, *126*, 219–223.

(10) Neek-Amal, M.; Peeters, F. M. *Phys. Rev. B* **2012**, *85*, 195445.

(11) Levy, N.; Burke, S. A.; Meaker, K. L.; Panlasigui, M.; Zettl, A.; Guinea, F.; Neto, A. H. C.; Crommie, M. F. *Science* **2010**, *329*, 544–547.

(12) Lu, J.; Neto, A.; Loh, K. *Nature Communications* **2012**, *3*, 823.

(13) Bao, Q.; Chen, J.; Xiang, Y.; Zhang, K.; Li, S.; Jiang, X.; Xu, Q.-H.; Loh, K. P.; Venkatesan, T. *Advanced Optical Materials* **2015**, *3*, 744–749.

(14) Cun, H.; Iannuzzi, M.; Hemmi, A.; Roth, S.; Osterwalder, J.; Greber, T. *Nano Letters* **2013**, *13*, 2098–2103.

(15) Cun, H.; Iannuzzi, M.; Hemmi, A.; Osterwalder, J.; Greber, T. *Surface Science* **2014**, *634*, 95–102.

(16) Cun, H.; Iannuzzi, M.; Hemmi, A.; Osterwalder, J.; Greber, T. *ACS Nano* **2014**, *8*, 1014–1021.

(17) Herbig, C.; Åhlgren, E. H.; Jolie, W.; Busse, C.; Kotakoski, J.; Krasheninnikov, A. V.; Michely, T. *ACS Nano* **2014**, *8*, 12208–12218.

(18) Locatelli, A.; Wang, C.; Africh, C.; Stojić, N.; Menteş, T. O.; Comelli, G.; Binggeli, N. *ACS Nano* **2013**, *7*, 6955–6963.

(19) Locatelli, A.; Zamborlini, G.; Menteş, T. O. *Carbon* **2014**, *74*, 237–248.

(20) Loginova, E.; Bartelt, N. C.; Feibelman, P. J.; McCarty, K. F. *New J. Phys.* **2009**, *11*, 063046.

(21) Li, Y.; Subramaniam, D.; Atodiresei, N.; Lazić, P.; Caciuc, V.; Pauly, C.; Georgi, A.; Busse, C.; Liebmann, M.; Blügel, S.; Pratzer, M.; Morgenstern, M.; Mazzarello, R. *Advanced Materials* **2013**, *25*, 1967–1972.

(22) Bauer, E. *Rep. Prog. Phys.* **1994**, *57*, 895.

(23) Locatelli, A.; Mentes, T. O. In *Synchrotron Radiation*; Mobilio, S., Boscherini, F., Meneghini, C., Eds.; Springer Berlin Heidelberg, 2015; pp 571–591.

(24) Åhlgren, E. H.; Hämäläainen, S. K.; Lehtinen, O.; Liljeroth, P.; Kotakoski, J. *Phys. Rev. B* **2013**, *88*, 155419.

(25) Imam, M.; Stojić, N.; Binggeli, N. *J. Phys. Chem. C* **2014**, *118*, 9514–9523.

(26) Ugeda, M. M.; Fernández-Torre, D.; Brihuega, I.; Pou, P.; Martínez-Galera, A. J.; Pérez, R.; Gómez-Rodríguez, J. M. *Phys. Rev. Lett.* **2011**, *107*, 116803.

(27) Standop, S.; Lehtinen, O.; Herbig, C.; Lewes-Malandrakis, G.; Craes, F.; Kotakoski, J.; Michely, T.; Krasheninnikov, A. V.; Busse, C. *Nano Letters* **2013**, *13*, 1948–1955.

(28) The protrusions ripen significantly at high temperature, when the BG phase is not found on the surface.

(29) Lahrood, A. R.; de los Arcos, T.; Prenzel, M.; von Keudell, A.; Winter, J. *Thin Solid Films* **2011**, *520*, 1625–1630.

(30) Biswas, C.; Shukla, A. K.; Banik, S.; Barman, S. R.; Chakrabarti, A. *Phys. Rev. Lett.* **2004**, *92*, 115506.

(31) Dhaka, R. S.; Biswas, C.; Shukla, A. K.; Barman, S. R.; Chakrabarti, A. *Phys. Rev. B* **2008**, *77*, 104119.

(32) Yamamoto, M.; Pierre-Louis, O.; Huang, J.; Fuhrer, M. S.; Einstein, T. L.; Cullen, W. G. *Phys. Rev. X* **2012**, *2*, 041018.

(33) Tchaplyguine, M.; Feifel, R.; Marinho, R.; Gisselbrecht, M.; Sorensen, S.; de Brito, A. N.; Mårtensson, N.; Svensson, S.; Björneholm, O. *Chemical Physics* **2003**, *289*, 3–13.

(34) Tanuma, S.; Powell, C. J.; Penn, D. R. *Surf. Interf. Anal.* **2011**, *43*, 689–713.

(35) From a separate calculation involving only graphene sheet, we find that roughly half of the energy gain (520 out of 1170 meV for Ar tetramer) is due to the change in the distortion/strain energy of graphene. The other part comes from the change in adhesion energy also related to the graphene distortion. We remark that the energy contribution due to the surface distortion of Ir is negligible since atomic displacements are very small ($\sim 0.05$ Å both laterally and vertically) and very local (limited to $\sim 2$ Ir atoms). .

(36) Gsell, M.; Jakob, P.; Menzel, D. *Science* **1998**, *280*, 717–720.

(37) For large $N$, the induced adhesion energy reduction is expected to scale as the base surface area of the 3D (2D) Ar clusters and the membrane strain energy for the 3D clusters is expected to scale as the external/protruding surface area of the cluster (the Ar/graphene contact area) .

(38) We note that the calculated bulk interatomic distance in fcc Ar, 3.82 Å, is relatively close to the equilibrium distance of the dimer in vacuum.

(39) The latter component of the stress gives us an estimate of the conditions to which small 3D clusters are subject. For the horizontal (2D) clusters, the corresponding stress components from the vertical forces acting on the Ar atoms in the frozen Ar/Ir(100) system without the graphene membrane are in the range 16-44 GPa. The 16 GPa value corresponds to the Ar tetramer and the 44 GPa value to the monomer.

(40) The effective pressures were evaluated, as in the macroscopic case, as one third of the trace of the stress tensor.

(41) Lacerda, R. G.; dos Santos, M. C.; Tessler, L. R.; Hammer, P.; Alvarez, F.; Marques, F. C. *Phys. Rev. B* **2003**, *68*, 054104.

(42) Boehler, R.; Ross, M.; Söderlind, P.; Boercker, D. B. *Phys. Rev. Lett.* **2001**, *86*, 5731–5734.

(43) Späth, F.; Gotterbarm, K.; Amende, M.; Bauer, U.; Gleichweit, C.; Höfert, O.; Steinrück, H.-P.; Papp, C. *Surface Science* **2015**, in press.

(44) Kim, H.; Ko, W.; Ku, J.; Jeon, I.; Kim, D.; Kwon, H.; Oh, Y.; Ryu, S.; Kuk, Y.; Hwang, S.; Suh, H. *Nature Communications* **2015**, *6*, 7528.

(45) Schmidt, T.; Heun, S.; Slezak, J.; Diaz, J.; Prince, K. C.; Lilienkamp, G.; Bauer, E. *Surf. Rev. Lett.* **1998**, *5*, 1287–1296.

(46) Locatelli, A.; Aballe, L.; Menteş, T. O.; Kiskinova, M.; Bauer, E. *Surf. Interf. Anal.* **2006**, *38*, 1554–1557.

(47) Menteş, T. O.; Zamborlini, G.; Sala, A.; Locatelli, A. *Beilstein Journal of Nanotechnology* **2014**, *5*, 1873–1886.

(48) Giannozzi, P.; Baroni, S.; Bonini, N.; Calandra, M.; Car, R.; Cavazzoni, C.; Ceresoli, D.; Chiarotti, G. L.; Cococcioni, M.; Dabo, I.; *et al.*, *J. Phys.: Condens. Matter* **2009**, *21*, 395502–395520.

(49) Perdew, J. P.; Burke, K.; Ernzerhof, M. *Phys. Rev. Lett.* **1996**, *77*, 3865–3868.

(50) Barone, V.; Casarin, M.; Forrer, D.; Pavone, M.; Sambi, M.; Vittadini, A. *J. Comput. Chem.* **2009**, *30*, 934–939.

(51) Grimme, S. *J. Comput. Chem.* **2006**, *27*, 1787–1799.

(52) Vanderbilt, D. *Phys. Rev. B* **1990**, *41*, 7892–7895.

(53) Tersoff, J.; Hamann, D. R. *Phys. Rev. Lett.* **1983**, *50*, 1998–2001.

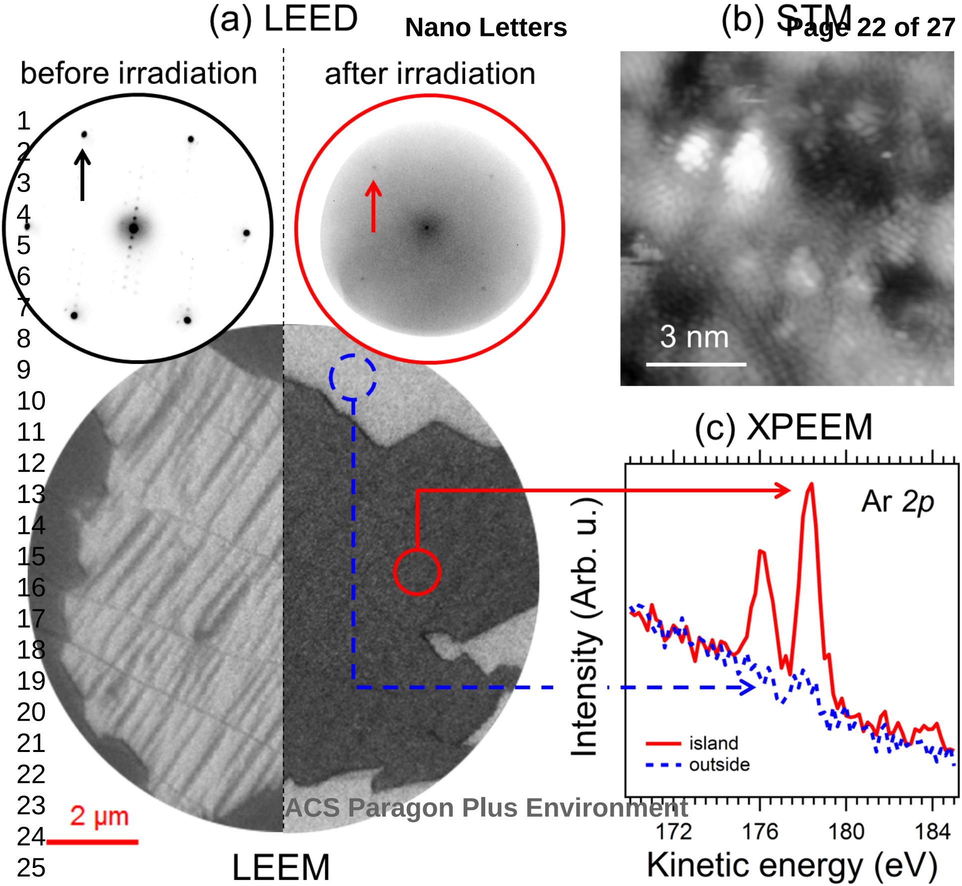
(a) LEED
before irradiation
after irradiation
2 μm
LEEM
(b) STM
3 nm
(c) XPEEM
Ar 2p
Intensity (Arb. u.)
island
outside
172
176
180
184
Kinetic energy (eV)

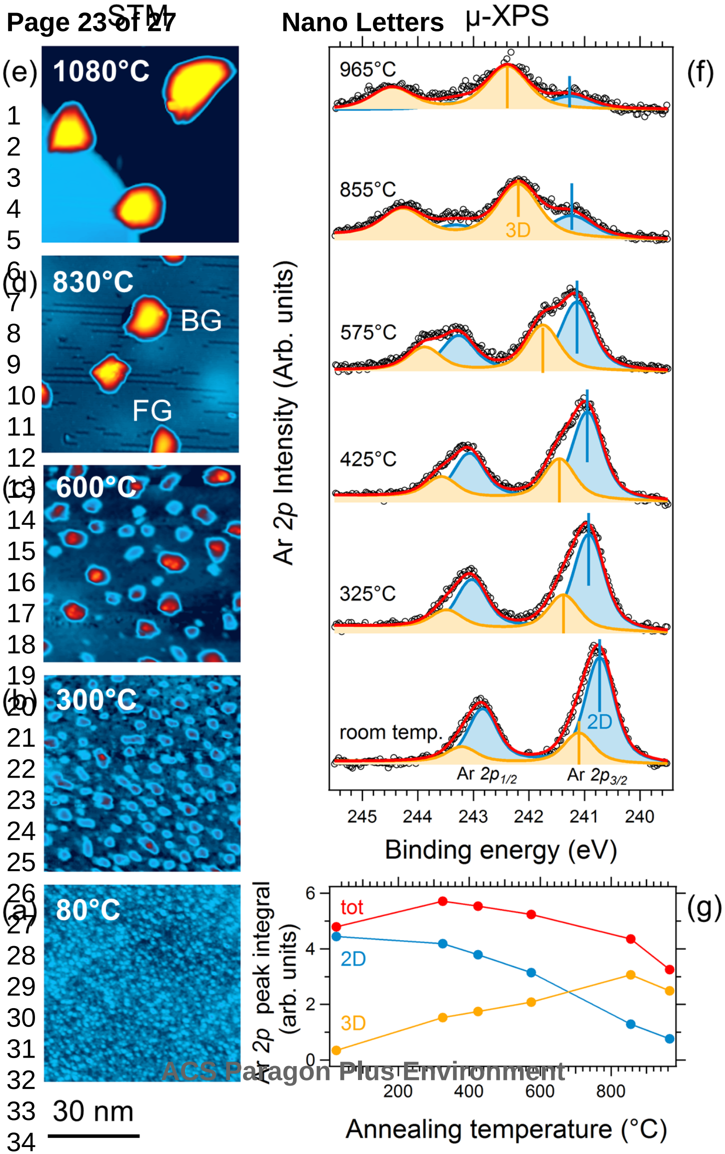
STM
μ-XPS
(e)
1080°C
(d)
830°C
BG
FG
(c)
600°C
(b)
300°C
(a)
80°C
30 nm
(f)
965°C
855°C
3D
575°C
425°C
325°C
room temp.
2D
Ar $2p_{1/2}$
Ar $2p_{3/2}$
245
244
243
242
241
240
Binding energy (eV)
Ar $2p$ Intensity (Arb. units)
(g)
tot
2D
3D
6
4
2
0
200
400
600
800
Ar $2p$ peak integral (arb. units)
Annealing temperature (°C)

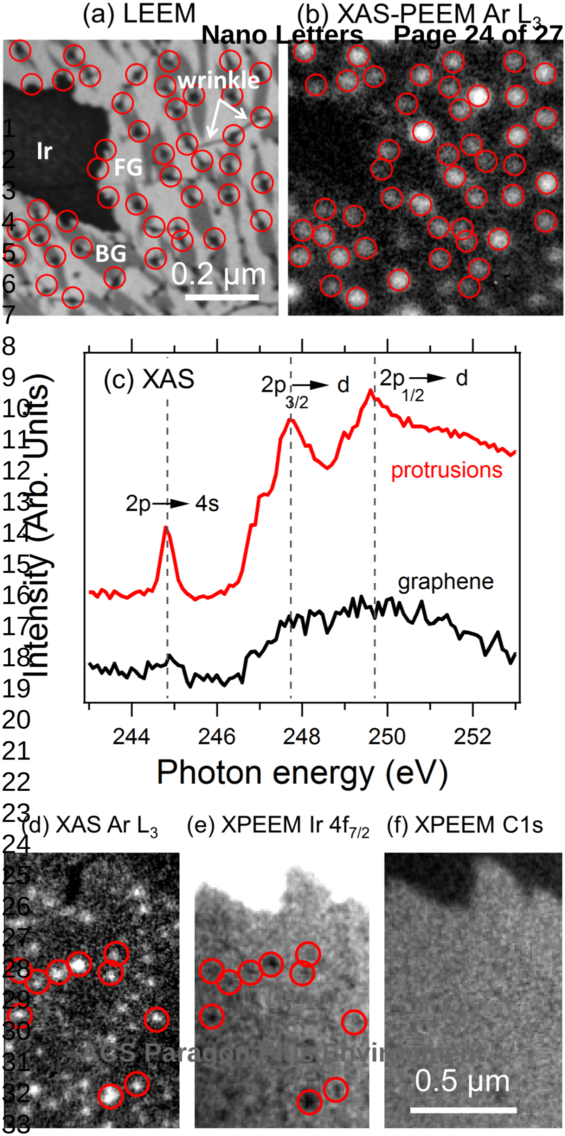
(a) LEEM
(b) XAS-PEEM Ar $L_3$
wrinkle
Ir
FG
BG
0.2 μm
(c) XAS
$2p_{3/2} \rightarrow d$
$2p_{1/2} \rightarrow d$
$2p \rightarrow 4s$
protrusions
graphene
Intensity (Arb. Units)
244
246
248
250
252
Photon energy (eV)
(d) XAS Ar $L_3$
(e) XPEEM Ir $4f_{7/2}$
(f) XPEEM C1s
0.5 μm

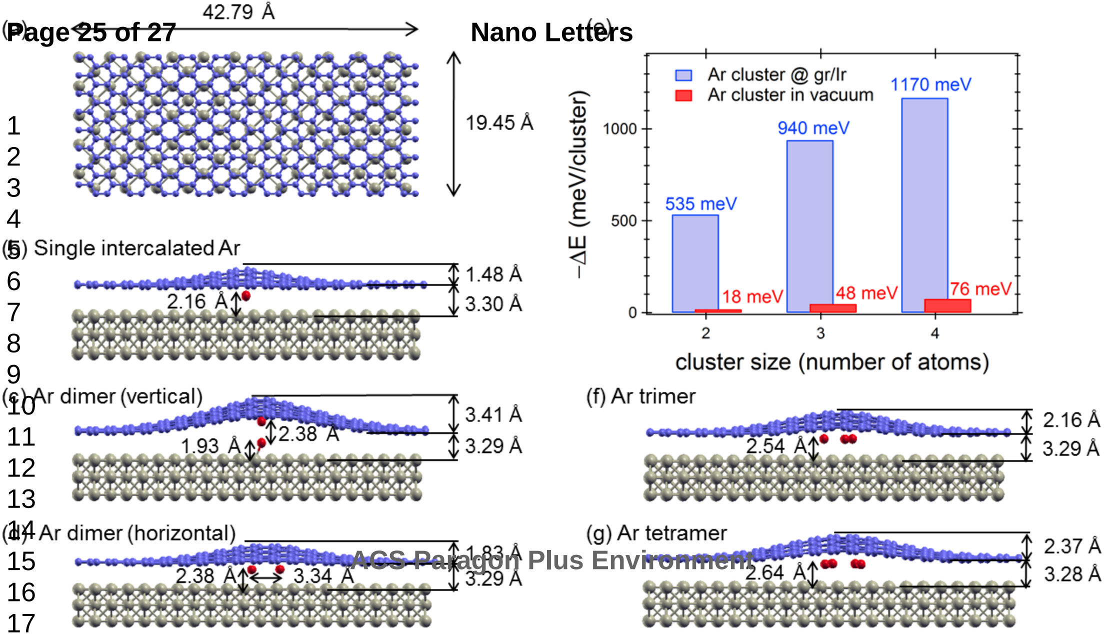
(a)
42.79 Å
19.45 Å
(b) Single intercalated Ar
1.48 Å
3.30 Å
2.16 Å
(c) Ar dimer (vertical)
3.41 Å
3.29 Å
2.38 Å
1.93 Å
(d) Ar dimer (horizontal)
1.83 Å
3.29 Å
2.38 Å
3.34 Å
(e)
Ar cluster @ gr/Ir
Ar cluster in vacuum
−ΔE (meV/cluster)
0
500
1000
535 meV
940 meV
1170 meV
18 meV
48 meV
76 meV
2
3
4
cluster size (number of atoms)
(f) Ar trimer
2.16 Å
3.29 Å
2.54 Å
(g) Ar tetramer
2.37 Å
3.28 Å
2.64 Å

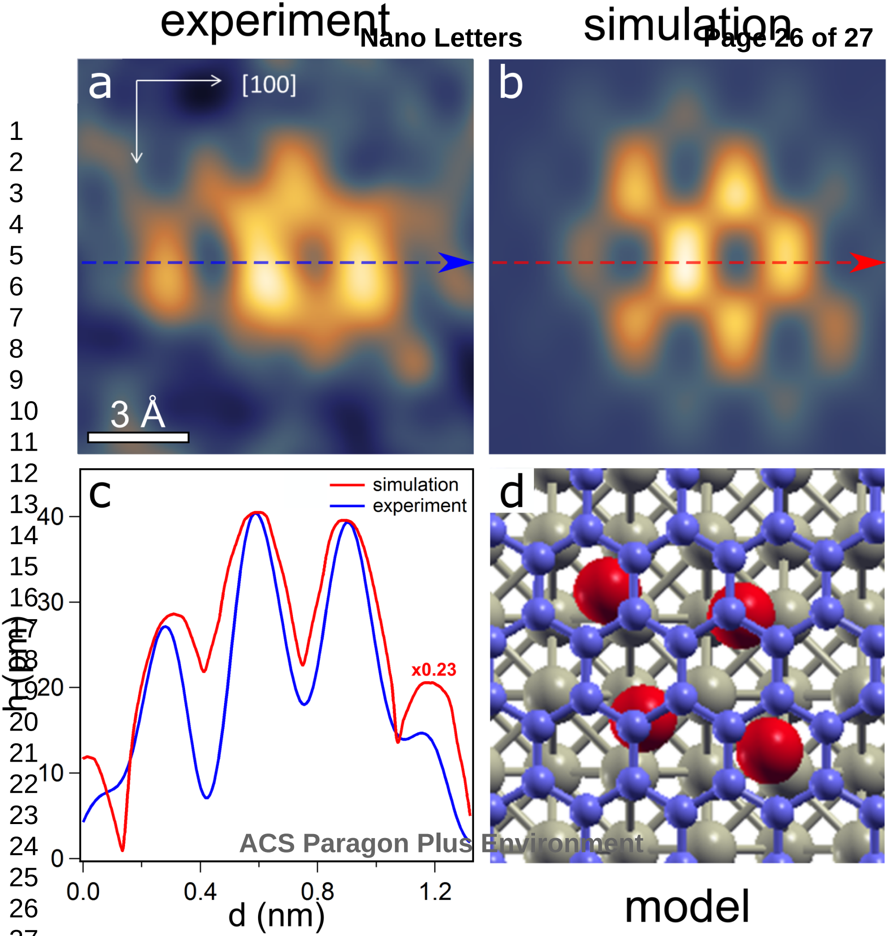
experiment
simulation
a
[100]
3 Å
b
c
simulation
experiment
h (pm)
40
30
20
10
0
x0.23
0.0
0.4
0.8
1.2
d (nm)
d
model

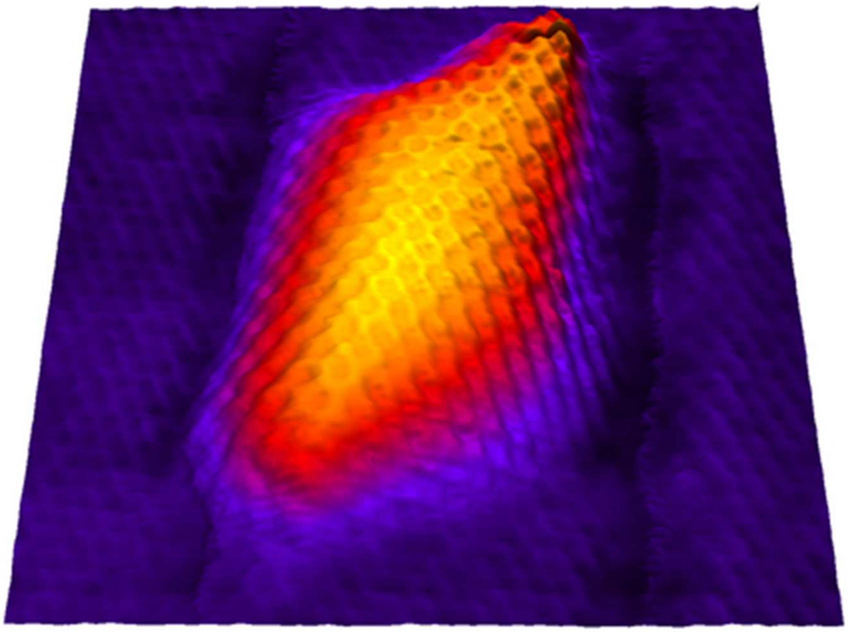

Table of Contents Graphic
39x27mm (300 x 300 DPI)